Quantitative three-dimensional photoacoustic tomography of the finger joints: an *in vivo* study

Yao Sun
University on Florida
Department of Biomedical Engineering
130 BME Building
P.O. Box 116131
Gainesville, Florida 32611

Eric Sobel
Universiry of Florida
Divison of Rheumatology
College of Medicine
Gainesville, Florida 32611

Huabei Jiang
University of Florida
Department of Biomedical Engineering
130 BME Building
P.O. Box 116131
Gainesville, Florida 32611

Abstract. We present for the first time *in vivo* full three-dimensional (3-D) photoacoustic tomography (PAT) of the distal interphalangeal joint in a human subject. Both absorbed energy density and absorption coefficient images of the joint are quantitatively obtained using our finite-element-based photoacoustic image reconstruction algorithm coupled with the photon diffusion equation. The results show that major anatomical features in the joint along with the side arteries can be imaged with a 1-MHz transducer in a spherical scanning geometry. In addition, the cartilages associated with the joint can be quantitatively differentiated from the phalanx. This *in vivo* study suggests that the 3-D PAT method described has the potential to be used for early diagnosis of joint diseases such as osteoarthritis and rheumatoid arthritis.
[DOI: 10.1117/1.3257246]

Keywords: three-dimensional; photoacoustic; arthritis.

Paper 09032R received Feb. 5, 2009; revised manuscript received May 26, 2009; accepted for publication Sep. 8, 2009; published online Nov. 4, 2009.

1 Introduction

Photoacoustic tomography (PAT), also referred as optoacoustic tomography (OAT), is an emerging nonionizing, noninvasive imaging modality, which combines both high optical contrast and high ultrasound resolution in a single modality.[1–3] Thus far, PAT has shown its potential to detect breast cancer, to assess vascular and skin diseases, and to image epilepsy in small animals.[4–13] By combining a light transport model with conventional PAT method,[14–18] the utility of PAT has now been extended significantly to provide quantitative tissue absorption coefficient and physiological/functional information including hemoglobin concentration, blood oxygenation, and water content. These intrinsic tissue properties may be important for accurate diagnostic decision-making.

Diseases related to bones and joints are a major cause of morbidity in the population over 50 year old and affect millions of people over the world, early detection of which is infeasible with traditional methods such as x-ray radiography, computed tomography (CT), and ultrasonography. Magnetic resonance imaging (MRI) represents a powerful tool for imaging joint diseases, but it is costly and cannot be used for frequent monitoring of the progressive joint diseases. Diffuse optical tomography (DOT), an emerging all-optical imaging modality, has been studied for joint imaging.[19–21] Significant absorption contrast between diseased and normal joints has been observed in the hand with osteoarthritis[22,23] and rheumatoid arthritis.[24,25] For example, for an osteoarthritic joint, the ratio of its cartilage absorption coefficient to that of the associated bone is increased by 40% relative to the healthy joints.[22] Since the same high absorption contrast is available to PAT, we expect that PAT may represent another optical-based modality for joint imaging with improved spatial resolution.

Wang et al.[26] have recently presented high-resolution two-dimensional (2-D) photoacoustic images of the proximal interphalangeal (PIP) and distal interphalangeal (DIP) joints from a cadaver human finger. *In vivo* joint imaging represents a challenge because unlike the joint from a cadaver finger, an *in vivo* joint has abundant blood vessels located along the skin that strongly absorb light. The strong absorption from the blood vessels and bones give rise to significantly reduced signal-to-noise ratio (SNR) in an *in vivo* setting. In addition, both light and acoustic propagation in tissue are 3-D in nature. In particular, the joint structures are highly heterogeneous, which makes a full 3-D volumetric image reconstruction necessary.

Herein, in this study, we present an *in vivo* full 3-D PAT study of the DIP joint in a human subject using a Ti:Sapphire laser–based photoacoustic system in a spherical scanning geometry. Photoacoustic images containing major features/components in the finger joint as well as the absorption coefficient profiles of these joint structures are successfully achieved.

2 Methods

The finite-element-based 3-D PAT reconstruction algorithm and its enhancement for extracting quantitative absorption coefficient used in this study have been described in detail previously and validated using considerable phantom experiments.[15,27,28] (We found that the accuracy for obtaining absorption coefficient from the phantom experiments is typically within 20% relative to the exact values.) Basically, the

Address all correspondence to: Huabei Jiang, University of Florida, Department of Biomedical Engineering, 130 BME Building, P.O. Box 116131, Gainesville, FL 32611. Tel: 352-392-7943; Fax: 352-392-9791; E-mail: hjiang@bme.ufl.edu

1083-3668/2009/14(6)/064002/5/$25.00 © 2009 SPIE

reconstruction method includes two steps. The first step is to obtain the 3-D images of absorbed optical energy density through the conventional 3-D PAT reconstruction algorithm that is based on finite element solution to the photoacoustic wave equation in the frequency-domain subject to the second-order absorption boundary conditions:[27]

$$\nabla^2 P(\vec{r},\omega) + k_0^2 P(\vec{r},\omega) = ik_0 \frac{c_0 \beta \phi(\vec{r})}{C_p}, \tag{1}$$

$$\nabla P \cdot \hat{n} = -MP, \tag{2}$$

where P is the pressure wave; $k_0 = \omega / c_0$ is the wave number described by the angular frequency, ω and the average speed of acoustic wave in the tissue, c_0; β is the thermal expansion coefficient; C_p is the specific heat at constant pressure; and ϕ is the absorbed light energy density. M is a differential operator defined as the function of the mean and Gaussian curvatures at a point along the boundary surface.

The reconstruction algorithm assumes a homogeneous acoustic speed c_0, which is an approximation to the possible heterogeneous acoustic media seen in the experiments. Newton method combined with Marquardt and Tikhonov regularizations is used to iteratively update an initial (guess) absorbed optical energy density distribution so that an object function composed of a weighted sum of the squared difference between computed and measured acoustic pressures for all acoustic frequencies can be minimized.

The second step is to recover the optical absorption coefficient using the absorbed optical energy density, ϕ reconstructed in the first step and the following photon diffusion equation as along with the Robin boundary conditions:[15]

$$\nabla \cdot D(\vec{r}) \nabla [\Psi(\vec{r})] - \mu_a(\vec{r}) \Psi(\vec{r}) = -S(\vec{r}), \tag{3}$$

$$-D \nabla \Psi(\vec{r}) \cdot \hat{n} = \alpha \Psi(\vec{r}), \tag{4}$$

where $\Psi(\vec{r})$ is the photon density, $\Psi(\vec{r}) = \phi(\vec{r}) / \mu_a(\vec{r})$, $\mu_a(\vec{r})$ is the optical absorption coefficient, $D(\vec{r})$ is the diffusion coefficient, $D = 1/[3(\mu_a + \mu_s')]$ and μ_s' is the reduced scattering coefficients, α is a boundary condition coefficient related to the internal reflection at the boundary, and $S(\vec{r})$ is the incident point or distributed source term.

To recover the optical absorption coefficient from the reconstructed absorbed optical energy density ϕ from an initial distribution of $\mu_a(\vec{r})$, the optical fluence $\Psi(\vec{r})$ and the absorbed energy density $\phi^{(c)}$ are iteratively calculated through the photon diffusion equation and $\phi^{(c)} = \mu_a(\vec{r})\Psi$, respectively. If the error between ϕ and $\phi^{(c)}$ is not small, then $\mu_a(\vec{r})$ is updated by $\mu_a(\vec{r}) = \phi / \Psi$, and the preceding procedure is repeated until a small error between ϕ and $\phi^{(c)}$ is reached, resulting in a stable quantitative distribution of $\mu_a(\vec{r})$.

3 System and Experiments

The *in vivo* finger joint experiment was conducted with our 3-D PAT imaging system, as shown in Fig. 1. The Ti:Sapphire laser (LOTIS, Minsk, Belarus) generates a pulsed beam with a repetition rate of 10 Hz and a pulse width <10 ns. The wavelength of the laser is tunable from 600 to 950 nm and was locked at 820 nm in this study for deep tissue penetration. The light beam is delivered via an optical fiber to the bottom of the water tank and expanded by a lens and a ground glass before reaching the finger so that the DIP joint can be uniformly illuminated by an area source of light. The laser energy at the DIP joint was controlled around 10 mJ/cm^2, which is far below the safety standard of 22 mJ/cm^2.

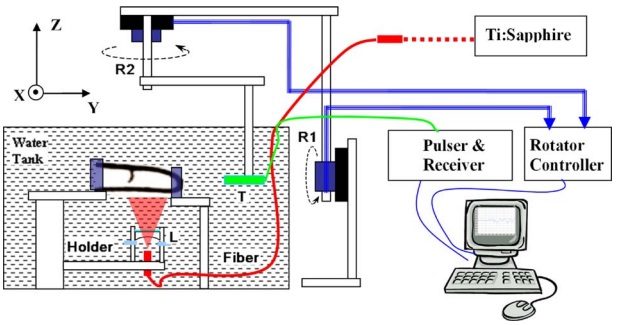

Fig. 1 Schematic of the 3-D spherical scanning PAT system for finger joint imaging. L: lens; T: detector/transducer; R1/R2: rotary stages.

The DIP joint of the left index finger from a female healthy volunteer was photoacoustically examined, and the palmar side of the finger faced up during the examination, allowing the finger joint to be illuminated from the dorsal side of the finger. Our experience indicates that this way of light illumination can give us maximized tissue penetration. To secure the position of the finger, rubber bands were applied to the distal tip and the proximal end of the examined finger.

To detect the acoustic field generated by the pulsed laser, 1-MHz transducer (Valpey Fisher, Hopkinton, Massachusetts) was optimally chosen based on considerable phantom experiments.[28] The transducer has a bandwidth of 80% at −6 dB and an aperture size of 6 mm. To overcome the directivity limitation and aperture size effect of transducer, we adopted a spherical scanning configuration. Both the transducer and the finger were immersed in the water tank for minimized ultrasound attenuation. As can be seen from Fig. 1, the transducer was attached to the rotary stage R2 whose position was controlled by the rotary stage R1. During the examination, the finger was placed at the center of the two rotary stages. The detected acoustic signals were amplified and filtered by a Pulser/Receiver 5058PR (Panametrics, Waltham, Massachusetts). Labview software was used to control the entire data acquisition procedure.

The collection of acoustic signals along a spherical scanning surface was realized through the combined rotations of rotary stages R1 and R2. (Note that R1 and R2 were attached to the same L-shape arm; see Fig. 1.) As shown in Fig. 2, the examined finger joint was aligned in the direction of y axis, and located at the rotation center, O. In the scanning, the transducer was first rotated by R1 to a position along the circular locus L1 and then rotated by R2 along the circular locus L2 [Fig. 2(a)]. This process was repeated until the spherical scanning was completed. Since the finger/hand blocked the scanning of the transducer in certain angles, the scanning along L1 and L2 covered only 240 deg and 252 deg, respectively [Figs. 2(b) and 2(c)]. A complete

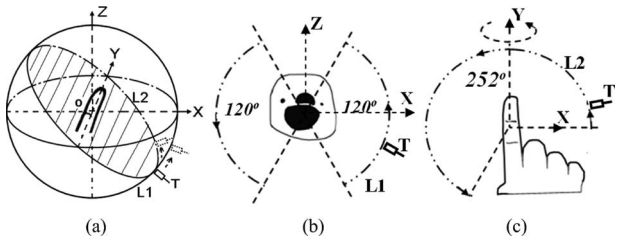

Fig. 2 Schematic of the spherical scanning geometry (a), circular locus L1 (b), and L2 (c).

scanning allowed the collection of signals at 387 positions along the spherical surface which took about 40 min.

4 Results and Discussion

In this section, we present the *in vivo* 3-D reconstruction results and make observations based on these results. The 3-D images were reconstructed using a finite element mesh of 41,323 tetrahedral elements and 7519 nodes, which required 120 min per iteration, for a total of 10 iterations on a parallel computer with 10 processors. Each of the processors worked at 2.2 GHz with 2-GB memory.

A coronal section of the reconstructed 3-D image (absorbed energy density) is shown in Fig. 3(a), while a similar section of the DIP joint from a typical human finger by MRI is given in Fig. 3(b) for comparison. As can be observed from Fig. 3(a), the cartilage/joint space is well differentiated from the adjacent distal phalanx (DP) and intermediate phalanx (IP). The recovered absorption coefficient image and the absorption coefficient profile along a transect $x=-2$ mm corresponding to the coronal slice shown in Fig. 3(a) are displayed in Figs. 4(a) and 4(b), respectively. We see that the absorption coefficient values of the phalanxes and cartilage/joint space are quantitatively consistent with that reported in the literature.[22,23] By estimating the full width at half maximum (FWHM) of the absorption coefficient profiles, the recovered thickness of cartilage/joint space was found to be 1.6 mm, which is in agreement with the actual size.

Figure 5(a) presents a cross section of the reconstructed 3-D image (absorbed energy density). Again, a similar cross section of the DIP joint from a typical human finger by MRI is shown in Fig. 5(b) for comparison. Comparing both Figs.

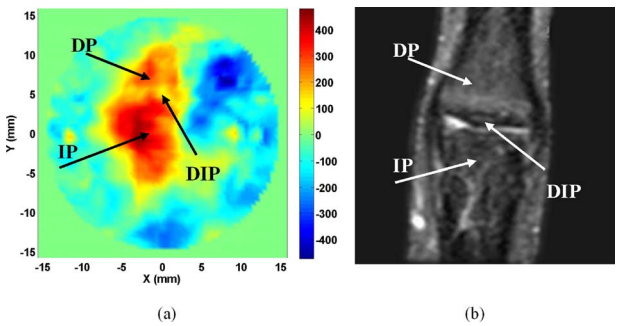

Fig. 3 Selected coronal section from the reconstructed 3-D image (absorbed energy density) at $z=-5$ mm (a), and MRI (coronal section) from a similar joint (b). DP: distal phalanx; IP: intermediate phalanx; DIP: distal interphalangeal joint.

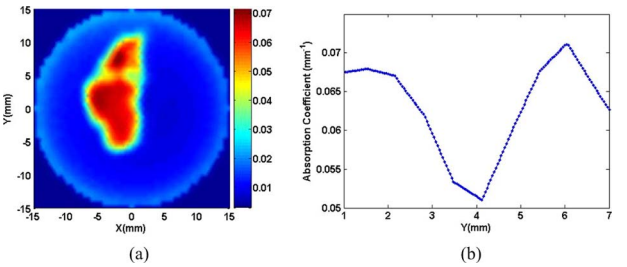

Fig. 4 Selected coronal section from the recovered absorption coefficient image at $z=-5$ mm (a), and its profile along the cut line $x=-2$ mm (b).

5(a) and 5(b), it appears that several joint tissue types are visible including phalanx (PX), lateral artery (LA), median artery (MA), and tendon (TE). The recovered absorption coefficient image and the absorption coefficient profiles along two transects are displayed in Figs. 6(a)–6(c). The first transect [line 1 in Fig. 6(a)] goes through the phalanx and tendon, while the second one [line 2 in Fig. 6(a)] crosses the tendon and two arteries. The recovered absorption coefficients of the phalanx, tendon, median and lateral arteries were found to be 0.07 mm^{-1}, 0.074 mm^{-1}, 0.064 mm^{-1}, and 0.058 mm^{-1}, respectively. Again, these values are generally consistent with that reported in the literature.[21,22] We note that blurs around the two blood vessels are noticeable [Fig. 5(a)] largely due to the relatively low-frequency (1 MHz) transducer used in this study. We believe the resolution can be enhanced with a wideband transducer having higher frequency (e.g., 5 to 10 MHz), which will make the millimeter- to submillimeter-sized arteries accurately imaged.

To view the volumetric structures of the tissues around the joint, a series of cross- and coronal-section images are displayed in Figs. 7 and 8, respectively. As shown in Figs. 7(a)–7(f), the phalanx is clearly visible in all the cross-section images from the proximal end ($y=-2.5$ mm) to the distal end ($y=9$ mm). The tendon is differentiated from the phalanx [Figs. 7(a), 7(e), and 7(f)]. The lateral artery is visible almost in all the cross section images except for that shown in Fig. 7(f) at the distal end of the finger. The median artery is seen in Figs. 7(e) and 7(f) and weakly visible in Fig. 7(d). Other joint structures including the phalanges (DP and IP) and the cartilage (CL) are clearly imaged from the coronal section images close to the dorsal side of the finger [Figs. 8(a) and 8(b)]. Close to the palmar side of the finger, the tendon and two arteries begin to show up [Fig. 8(c)], and the two arteries become clearly visible eventually [Fig. 8(d)]. Negative values are also observed in the reconstructed absorbed energy density images. This is likely due to the homogenous acoustic approximation (constant acoustic speed) to the actual heterogeneous acoustic media of the finger joints and limited signal-to-noise ratio because of the strong light scattering of joint tissues.

In summary, we have presented a 3-D PAT technique that is able to image finger joints *in vivo*. Although it seems impossible for PAT to provide image quality (in terms of spatial resolution) comparable to MRI for joint or breast imaging, PAT is capable of obtaining absorption coefficient or functional information. In addition, PAT is portable and low in

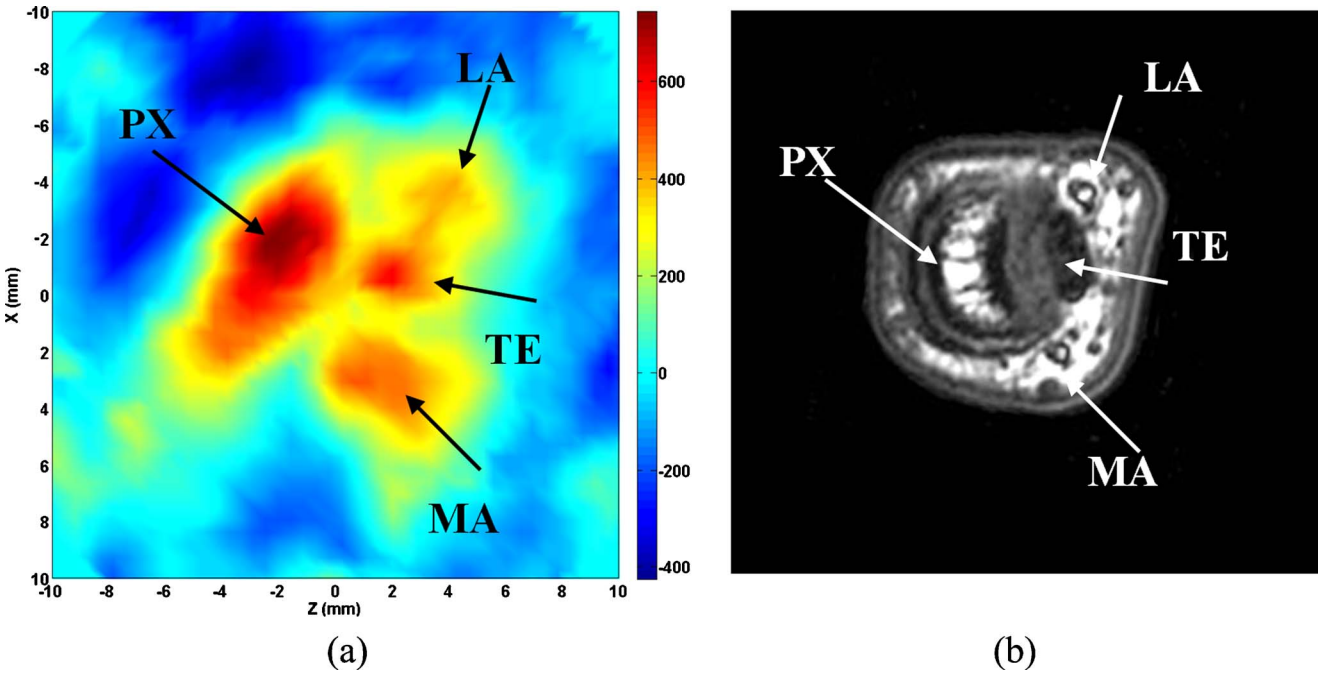

Fig. 5 Selected cross section from the reconstructed 3-D image (absorbed energy density) at $y=7$ mm (a), and MRI (cross section) from a similar joint (b). PX: phalanx; MA: median artery; TE: tendon; LA: lateral artery.

cost. While our current experimental setup is not optimized, it allows us to demonstrate the possibility of 3-D *in vivo* joint imaging for the first time. The results obtained indicate that major joint structures and their absorption coefficients can be quantitatively reconstructed using our 3-D PAT approach. We plan to improve our imaging system for optimized performance. For example, we will implement an excitation configuration that allows light illumination of the entire finger joint, which would then permit the use of higher frequency transducers for enhanced resolution due to the significantly

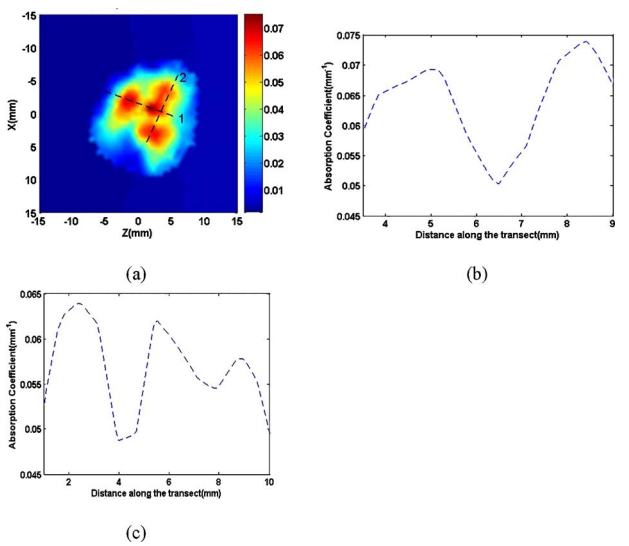

Fig. 6 Selected cross section from the recovered absorption coefficient image at $y=7$ mm (a), and its profile along cut lines 1 (b) and 2 (c), respectively.

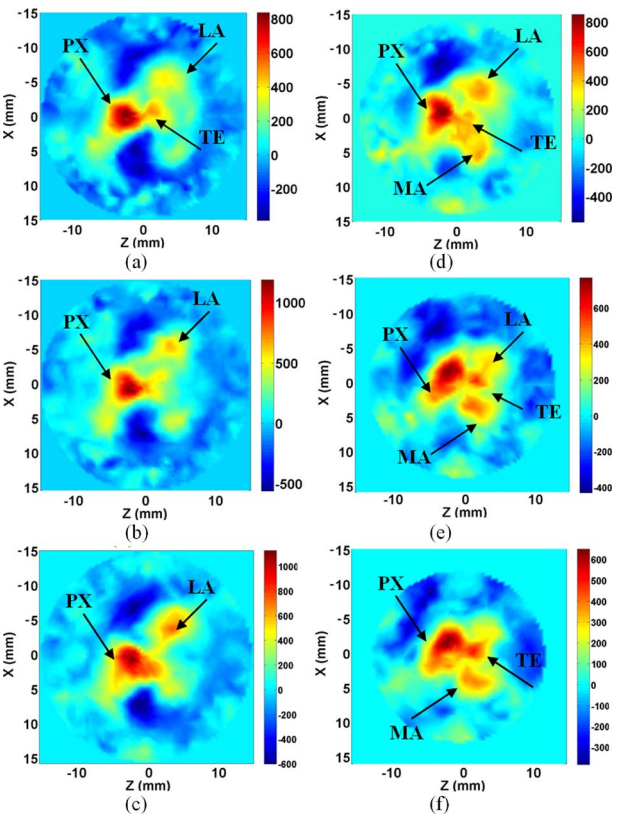

Fig. 7 Cross-section images (absorbed energy density) at $y=-2.5$ mm (a), $y=0$ mm (b), $y=3$ mm (c), $y=5$ mm (d), $y=7$ mm (e), and $y=9$ mm (f). PX: phalanx; MA: median artery; TE: tendon; LA: lateral artery.

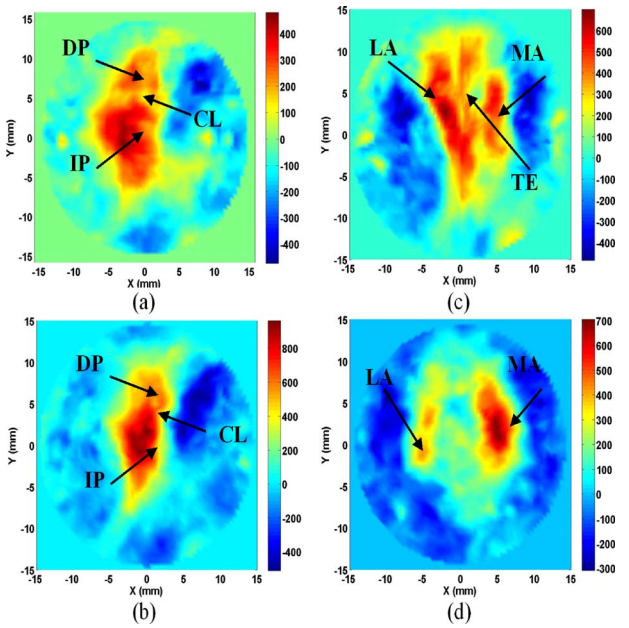

Fig. 8 Coronal-section images (absorbed energy density) at $z=-5$ mm (a), $z=-3.5$ mm (b), $z=1$ mm (c), and $z=4.5$ mm (d). DP: distal phalanx; IP: intermediate phalanx; CL: cartilage; PX: phalanx; MA: median artery; TE: tendon; LA: lateral artery.

improved signal-to-noise ratio. We also plan to perform *in vivo* 3-D PAT studies in human subjects with hand osteoarthritis or rheumatoid arthritis in the near future.

References

1. A. A. Oraevsky and A. A. Karabutov, "Optoacoustic tomography," Chapter 34 in *Biomedical Photonics Handbook*, T. Vo-Dinh, Ed., Vol. **PM125**, pp. 34/1–34/34 CRC Press, Boca Raton, FL (2003).
2. A. A. Oraevsky, S. L. Jacques, R. O. Esenaliev, and F. K. Tittel, "Laser based optoacoustic imaging in biological tissues," *Proc. SPIE* **2134A**, 122–128 (1994).
3. R. A. Kruger and P. Liu, "Photoacoustic ultrasound reconstruction tomography," *Med. Phys.* **22**(10), 1605–1609 (1995).
4. A. A. Oraevsky, A. A. Karabutov, and S. V. Solomatin, "Laser optoacoustic imaging of breast cancer *in vivo*," *Proc. SPIE* **4256**, 6–11 (2001).
5. S. Manohar, A. Kharine, J. C. G. van Hespen, W. Steenbergen, and T. G. van Leeuwen, "Photoacoustic mammography laboratory prototype: imaging of breast tissue phantoms," *Phys. Med. Biol.* **50**, 2543–2557 (2005).
6. R. G. M. Kollkman, J. H. G. M. Klaessens, E. Hondebrink, J. C. W. Hopman, F. F. M. de Mul, W. Steenbergen, J. M. Thijssen, and T. G. V. Leeuwen, "Photoacoustic determination of blood vessel diameter," *Phys. Med. Biol.* **49**, 4745–4756 (2004).
7. R. I. Siphanto, K. K. Thumma, R. G. M. Kolkman, T. G. van Leeuwen, F. F. M. de Mul, J. W. van Neck, L. N. A. van Adrichem, and W. Steenbergen, "Serial noninvasive photoacoustic imaging of neovascularization in tumor angiogenesis," *Opt. Express* **13**, 89–95 (2005).
8. S. Yang, D. Xing, Q. Zhou, L. Xiang, and Y. Lao, "Functional imaging of cerebrovascular activities in small animals using high-resolution photoacoustic tomography," *Med. Phys.* **34**, 3294–3301 (2007).
9. X. Wang, Y. Pang, G. Ku, X. Xie, G. Stoica, and L. V. Wang, "Noninvasive laser-induced photoacoustic tomography for structural and functional *in vivo* imaging of the brain," *Nat. Biotechnol.* **21**, 803–806 (2003).
10. E. Z. Zhang, J. Laufer, and P. Beard, "Three-dimensional photoacoustic imaging of vascular anatomy in small animals using an optical detection system," *Proc. SPIE* **6437**, 643710 (2007).
11. A. A. Karabutov, E. Savateeva, and A. Oraevsky, "Imaging of layered structures in biological tissues with opto-acoustic front surface transducer," *Proc. SPIE* **3601**, 284–295 (1999).
12. J. A. Viator, G. Au, G. Paltauf, S. Jacques, S. Prahl, H. Ren, Z. Chen, and J. Nelson, "Clinical testing of a photoacoustic probe for port wine stain depth determination," *Lasers Surg. Med.* **30**, 141–148 (2002).
13. Q. Zhang, Z. Liu, P. R. Carney, Z. Yuan, H. Chen, S. N. Roper, and H. Jiang, "Non-invasive imaging of epileptic seizures *in vivo* using photoacoustic tomography," *Phys. Med. Biol.* **53**, 1921–1931 (2008).
14. J. Ripoll and V. Ntziachristos, "Quantitative point source photoacoustic inversion formulas for scattering and absorbing medium," *Phys. Rev. E* **71**, 031912 (2005).
15. Z. Yuan and H. Jiang, "Quantitative photoacoustic tomography: recovery of optical absorption coefficient map of heterogeneous medium," *Appl. Phys. Lett.* **88**, 231101 (2006).
16. B. Cox, S. Arridge, K. Kostli, and P. Beard, "2D quantitative photoacoustic image reconstruction of absorption distributions in scattering medium using a simple iterative method," *Appl. Opt.* **45**, 1866–1875 (2006).
17. L. Yin, Q. Wang, Q. Zhang, and H. Jiang, "Tomographic imaging of absolute optical absorption coefficient in turbid medium using combing photoacoustic and diffusing light measurements," *Opt. Lett.* **32**, 2556–2558 (2007).
18. Z. Yuan, Q. Wang, and H. Jiang, "Reconstruction of optical absorption coefficient maps of heterogeneous media by photoacoustic tomography coupled with diffusion equation based regularized Newton method," *Opt. Express* **15**, 18076–18081 (2007).
19. A. Klose, A. Hielscher, K. Hanson, and J. Beuthan, "Two- and three-dimensional optical tomography of finger joints for diagnostics of rheumatoid arthritis," *Proc. SPIE* **3566**, 151–159 (1998).
20. Y. Xu, N. Iftimia, and H. Jiang, "Imaging of *in vitro* and *in vivo* bones and joints with continuous-wave diffusion optical tomography," *Opt. Express* **8**, 447–451 (2001).
21. Y. Xu, W. Iftimia, H. Jiang, L. L. Key, and M. B. Bolster, "Three-dimensional diffuse optical tomography of bones and joints," *J. Biomed. Opt.* **7**, 88–92 (2002).
22. Z. Yuan, Q. Zhang, E. Sobel, and H. Jiang, "Three-dimensional diffuse optical tomography of osteoarthritis: initial results in the finger joints," *J. Biomed. Opt.* **12**, 034001-1–11 (2007).
23. Z. Yuan, Q. Zhang, E. S. Sobel, and H. Jiang, "Tomographic x-ray guided three-dimensional diffuse optical tomography of osteoarthritis in the finger joints," *J. Biomed. Opt.* **13**, 044006-1–10 (2008).
24. A. H. Hielscher, A. D. Klose, A. K. Scheel, B. Moa-Anderson, M. Backhaus, U. Netz, and J. Beuthan, "Sagittal laser optical tomography for imaging of rheumatoid finger joints," *Phys. Med. Biol.* **49**, 1147–1163 (2004).
25. A. K. Scheel, M. Backhaus, A. Klose, B. Moa-Anderson, U. Netz, K. Hermann, J. Beauthan, G. Muller, G. Brrmester, and A. Hielscher, "First clinical evaluation of sagittal laser optical tomography for detection of synovitis in arthritic finger joints," *Ann. Rheum. Dis.* **64**, 239–245 (2005).
26. X. Wang, D. L. Chamberland, and D. A. Jamadar, "Noninvasive photoacoustic tomography of human peripheral joints toward diagnosis of inflammatory arthritis," *Opt. Lett.* **32**, 3002–3004 (2007).
27. Z. Yuan and H. Jiang, "Three-dimensional finite-element-based photoacoustic tomography: reconstruction algorithm and simulations," *Med. Phys.* **34**, 538–546 (2007).
28. Y. Sun and H. Jiang, "Quantitative three-dimensional photoacoustic tomography of the finger joints: phantom studies in a spherical scanning geometry," *Phys. Med. Biol.* **54**, 5457–5467 (2009).